Examining the Source Regions of Solar Energetic Particles Using an AI-generated Synchronic Potential Field Source Surface Model

Jinhye Park[1] , Hyun-Jin Jeong[1] , and Yong-Jae Moon[1,2]
[1] Department of Astronomy and Space Science, Kyung Hee University, Yongin, 17104, Republic of Korea
[2] School of Space Research, Kyung Hee University, Yongin, 17104, Republic of Korea

Abstract

We study the source regions of six solar energetic particle (SEP) events accelerated near or behind the limbs of the Sun. We use AI-generated farside magnetograms at a near real-time basis developed by Jeong et al. and AI_{HMI}-PFSS extrapolations up to $2.5R_{\odot}$ computed using the input of the synchronic data combining AI-generated farside and HMI magnetograms. By comparing the AI_{HMI}, HMI, Global Oscillations Network Group (GONG) synoptic magnetograms, and Air force Data Assimilative Photospheric flux Transport synchronic magnetograms, as well as the PFSS extrapolations, we find interesting differences between them in view of SEP source regions and magnetic field configurations. First, the structures and sizes of the source active regions (ARs) are changed. The total unsigned magnetic field fluxes of the ARs are mostly stronger in the AI_{HMI} than in the HMI and GONG magnetograms. Second, newly emerging ARs are observed in the SEP source regions in the AI_{HMI} magnetograms for two events. Third, the alterations in the magnetic flux, the emergence, and the dissipation of ARs lead to modifications in the locations of the global polarity inversion lines (PILs). The EUV wave propagation is typically observed to be oriented nearly perpendicular with respect to the local PIL, suggesting that the AI_{HMI}-PFSS extrapolations around the source region are more realistic. This study shows that the continuous farside evolution of AR magnetic fields, which is accomplished by our AI synchronic magnetograms, can lead to an improved understanding of SEP source ARs.

1. Introduction

Solar energetic particles (SEPs) consist of protons, electrons, and heavy ions with an energy range from a few hundred keV to MeV. They are accelerated in magnetic reconnection regions and by coronal mass ejection (CME)-driven shocks (Kahler 1994; Reames 1999; Kallenrode 2003; Cane et al. 2006; Tylka & Lee 2006; Gopalswamy et al. 2008; Reames 2013). There are two types of SEP events, impulsive and gradual. Impulsive events are related to jets having open field lines and type III radio emissions. They generally have a narrow cone of emission and short durations of several hours. They are electron-rich and show enhanced Fe/O and $^{3}He/^{4}He$ compared with the nominal coronal abundances (Bučík 2020; Reames 2020). Meanwhile, gradual events are mainly accelerated by wide and fast CME-driven shocks (Kahler 2001; Gopalswamy 2003; Park et al. 2012; Kahler & Vourlidas 2013; Park et al. 2013, 2015). They are typically associated with gradual X-ray flares, type II, and type IV radio emissions. They have larger emission cones and longer durations than those in impulsive events (Kahler 1994; Reames 1999). Gradual events are proton-rich, and ion compositions exhibit typical coronal abundances (Reames 1998). Reames (2020) recently distinguished four SEP populations based on abundance patterns of chemical elements. In addition to pure impulsive and general gradual events, two more mixed types are suggested: impulsive events with ions accelerated by narrow CME shocks from jets and gradual events with remnant ions accelerated by multiple jets. The SEP events are one of the crucial phenomena in terms of space weather. They are likely to have large fluences and can pose serious radiation hazards.

Potential field source surface (PFSS) models extrapolate the large-scale solar magnetic fields in the corona using the photospheric observations (Altschuler & Newkirk 1969; Schatten et al. 1969; Riley et al. 2006). These models are widely used to examine the structure of the magnetic fields with diverse solar activities and provide the input data of heliospheric propagation models such as WSA-ENLIL (Arge & Pizzo 2000). Conventional synoptic maps of the magnetic field lines are constructed by merging frontside magnetograms near the central meridian over one synodic solar rotation period of 27.3 days. The farside data was obtained when it was near the central meridian a few weeks earlier. Recently, Laker et al. (2021) investigated the solar wind structure and heliospheric current sheet (HCS) using multiple observations with latitude across two solar rotations between May and July 2020 during solar minimum. They showed that the HCS structure obtained from the variation in magnetic polarity observation are flat within $\pm 10°$ latitude and they were broadly consistent with the shape of the HCS from the conventional PFSS extrapolation.

Jeong et al. (2020) generated the solar farside magnetograms using Solar Terrestrial Relations Observatory (STEREO)/ Extreme UltraViolet Imager (EUVI; Howard et al. 2008) A and B extreme ultraviolet (EUV) images (304, 195, and 171 Å) by a Pix2PixHD model, which is a deep-learning method for image translation of high-resolution images, with Solar Dynamics Observatory (SDO)/Atmospheric Imaging Assembly (AIA; Lemen et al. 2012) EUV images and Helioseismic and Magnetic Imager (HMI; Howard et al. 2008)

magnetograms. They made global magnetic field synchronic maps replaced by AI-generated farside magnetic fields on a near real-time basis. They showed that synchronic maps are more consistent with coronal observations compared with conventional maps in view of the distributions of solar active regions (ARs) and open magnetic field regions. Recently, Jeong et al. (2022) improved AI-generated solar farside magnetograms and generated more realistic magnetograms than the previous model. They used updated objective functions, which include correlation coefficients (CCs) between the real and generated data, as well as the construction of input data sets: STEREO EUV observations together with nearest frontside SDO data pairs of EUV observations and magnetograms. The improved model shows the high CCs (0.7–0.9) between real and AI-generated magnetograms for full disk, ARs, and quiet regions. The total unsigned magnetic flux and net magnetic flux of the AI-generated magnetograms are well consistent with those in the real magnetograms. Currently, the farside magnetograms by this method are released at http://sdo.kasi.re.kr.

In this study, we examine the magnetic field configurations of the source regions and global configurations for six SEP events accelerated near the eastern limb or behind the limbs, where the conventional PFSS models use photospheric magnetic data taken a few weeks ago. The six events were detected between 2010 and 2014 when solar activities increased. We use the synchronic magnetograms combining AI-generated farside magnetograms and HMI magnetograms (hereafter AI_{HMI} magnetograms), and the global coronal field extrapolations up to $2.5R_{\odot}$ driven by the AI_{HMI} magnetograms (hereafter AI_{HMI} extrapolation). We use the HMI and Global Oscillations Network Group (GONG) synoptic maps, as well as the PFSS extrapolations from the magnetograms compared with the AI_{HMI} ones. We also use data obtained from Air force Data Assimilative Photospheric flux Transport (ADAPT) model, which is a synchronic model that is based on localized ensemble Kalman filtering techniques (Hickmann et al. 2015). The model includes the effects of differential rotation, meridional flow, supergranulation, and random background flux. In the period between 2010 and 2014, the ADAPT model from the HMI magnetograms was not available, and so we use GONG magnetograms instead. Using the AI_{HMI}, the HMI, the GONG, and the surface flux transport magnetograms, we examine the magnetic field structures and strengths of SEP source regions and global configurations. The field connections between the sources and the source surface magnetic footpoints, as well as the global polarity inversion lines (PILs) are investigated using the PFSS extrapolations. The source surface magnetic footpoints of the spacecraft are estimated at $2.5R_{\odot}$ based on Parker spiral approximation and ballistic backmapping method (Nolte & Roelof 1973; Badman et al. 2020; Macneil et al. 2022). The structure of this paper is given as follows. We describe the data and analysis in Section 2, and we give the results in Section 3. The summary and discussion are given in Section 4.

2. Data and Analysis

We consider SEP events from 2010 to 2014 where STEREO-A, STEREO-B, and SDO were sufficiently well separated in the ecliptic plane to provide full-Sun EUV coverage. This allows the production of synchronic EUV maps directly from observations (using STEREO/EUVI and SDO/

AIA), and therefore the production of synchronic AI_{HMI} maps for this time interval (Jeong et al. 2020, 2022). We use NOAA solar proton events,[3] with SEP fluxes greater than or equal to 10 pfu in > 10 MeV proton channel measured by GOES between 2010 and 2014. We also use proton fluxes in the ranges of 1.8–60 MeV in STEREO Low Energy Telescope (LET; Mewaldt et al. 2008) and High Energy Telescope (HET; vonRosenvinge et al. 2008), 4.2–200 MeV in GOES15 Energetic Proton, Electron and Alpha Detector (EPEAD), and 2.11–67.3 MeV in SOHO Energetic and Relativistic Nuclei and Electron (ERNE; Torsti et al. 1995). We exclude events with complex flux profiles due to multiple SEP events and interplanetary shocks. We use the IP shock lists for ACE and WIND,[4] STEREO,[5] database of interplanetary shocks,[6] and Near-Earth Interplanetary Coronal Mass Ejections list.[7] From this analysis, we obtain 27 events and examine their magnetograms and PFSS extrapolations. Of the 27 events, we selected six events whose source regions were located at or near the solar limbs, and exhibited significant morphological differences in the resulting AI_{HMI} magnetograms compared to HMI, GONG, and ADAPT magnetograms for the same intervals.

Table 1 shows the six events that are studied in this paper and their associated solar activity. All six events have previously been associated with a specific source active region located on the farside or near the east limb. Hereafter, the events of 2011 September 21, 2011 September 22, 2012 September 27, 2013 March 5, 2013 June 21, and 2014 January 6 are termed the N1, N2, N3, N4, N5, and N6 events, respectively. Flare information is taken from ftp://ftp.ngdc.noaa.gov/STP/space-weather/solar-data/solar-features/solar-flares/x-rays/goes. Locations of the non-reported X-ray flares are examined in the full-Sun EUV Stonyhurst Heliographic images composed of STEREO/EUVI 195 Å images and SDO/AIA 193 Å images with a cadence of 5 minutes. In the apparent locations based on EUV synchronic maps in Figure 1, four of the event's source regions were located behind the limbs (N1 at $W120°$, N3 at $W150°$, N4 at $E150°$, and N6 at $W110°$). The remaining two were on disk near the east limb (N2 at $E74°$ and N5 at $E73°$) and they were associated with X1.4 and M2.9 flares, respectively. CME information is taken from http://cdaw.gsfc.nasa.gov/CME_list. All the events are associated with fast CMEs over 1000 km s^{-1}. Three of the events (N2, N5, and N6) are included in the NOAA solar proton event list (see footnote 3).

Table 1 also shows the onset times of the SEP fluxes events and peak times (fluxes) measured by 6-10 MeV proton channel of the STEREO/LET and 8.7–14.5 MeV proton channel of the GOES/EPEAD. All six events are detected in situ by multiple spacecraft (see column 12). The quoted times and peak fluxes in Table 1 are taken from the spacecraft whose source surface footpoints are closest to the source regions. The peak fluxes are measured as the points at the top of the of the steep flux rise just after the solar eruptions associated the SEP events.

In this study, we use the improved AI-generated solar farside magnetograms of Jeong et al. (2022), as follows. First, we
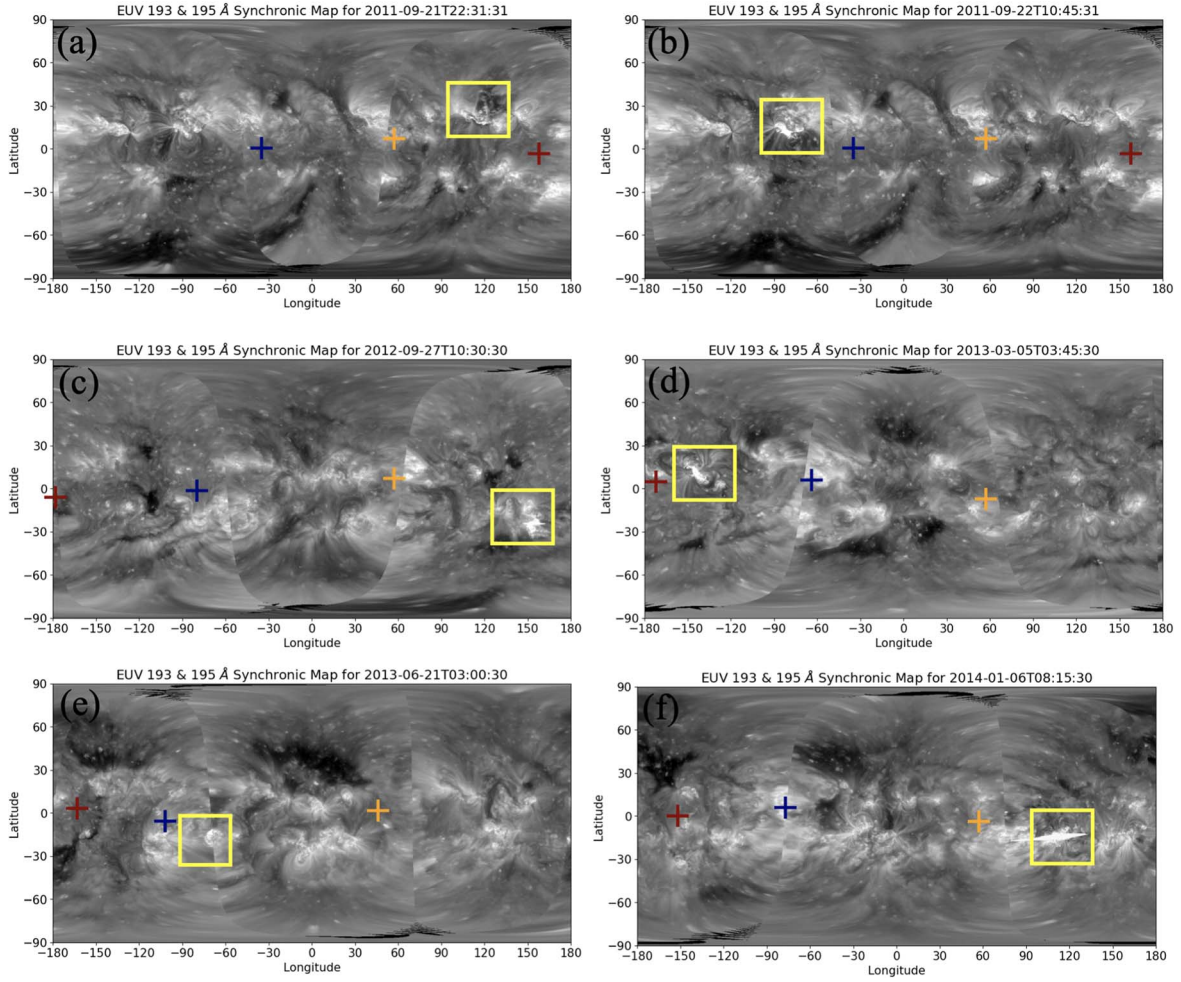

Figure 1. The running difference images from the composite of STEREO-A, B EUVI 195 Å, and SDO AIA 193 Å images at the times given. The source regions are enclosed by the yellow squares. The red, blue, and yellow crosses mark the magnetic footpoints of STEREO-A, B, and Earth at $2.5R_\odot$. (a) the N1 event (2011 September 21), (b) the N2 event (2011 September 22), (c) the N3 event (2012 September 27), (d) the N4 event (2013 March 5), (e) the N5 event (2013 June 21), and (f) the N6 event (2014 January 6).

Table 1
The Associated Solar Activities for the Six SEP Events, the SEP Onset Times, and the Peak Times

No. (1)	Date (2)	Flare[a] Peak (3)	Class (4)	Location (5)	AR (6)	CME[b] Time (7)	$V(\mathrm{km\ s^{-1}})$ (8)	AW(°) (9)	SEP[c] Start (10)	Peak (11)	In Situ (12)
N1	20110921	⋯	⋯	W120	11289	22:12	1007	>255	22 01:20UT	22 05:00UT (0.838)	S,A̲
N2	20110922[d]	11:01	X1.4	N11E74	11302	10:48	1905	360	22 11:20UT	22 22:50UT (297.730)	B,S(G̲),A
N3	20120927	⋯	⋯	W150	⋯	10:12	1319	360	27 12:40UT	27 18:30UT (30.836)	B,S(G),A̲
N4	20130305	⋯	⋯	E150	⋯	03:48	1316	360	5 04:30UT	5 09:20UT (175.340)	B,S,A̲
N5	20130621[d]	03:14	M2.9	S16E73	11777	03:12	1900	207	21 04:10UT	21 18:50UT (14.789)	B̲,S(G̲),A
N6	20140106[d]	⋯.	⋯	W110	11936	08:00	1402	360	6 09:50UT	6 12:25UT (1.710)	B,S(G̲),A

Notes. AW denotes CME angular width. G, S, A, and B represent GOES/EPEAD, SOHO/EREN, STEREO-A/LET, and STEREO-B/LET, respectively. The quoted times and peak fluxes are taken from the spacecraft (underlines in the column 12) whose source surface footpoints are closest to the source regions.
[a] Flare information is taken from ftp://ftp.ngdc.noaa.gov/STP/space-weather/solar-data/solar-features/solar-flares/x-rays/goes. Locations for farside SEP events (no flare data) are estimated using full-Sun EUV Stonyhurst Heliographic images composed of STEREO Extreme Ultraviolet Imager EUVI 195 Å images and SDO/AIA 193 Å images with a cadence of 5 minutes.
[b] CME information is taken from http://cdaw.gsfc.nasa.gov/CME_list and http://secchi.nrl.navy.mil/cactus.
[c] The peak fluxes in the fourth column are measured as the points at the top of the of the steep flux rise in the 6–10 MeV proton channel of the STEREO/LET and 8.7–14.5 MeV proton channel of the GOES/EPEAD. Flux unit is $\mathrm{cm^{-2}\ s^{-1}\ sr^{-1}\ MeV^{-1}}$.
[d] The events are in the NOAA solar proton event list (https://umbra.nascom.nasa.gov/SEP/).

convert the AI-generated ones from full disk data to heliographic coordinated maps. Second, we convert from the line of sight to the radial magnetic fields by applying the radial-acute method (Wang & Sheeley 1992) based on their coordinates. Third, we make HMI and AI synchronic data by replacing a farside part (Stonyhurst heliographic longitude $\geqslant |60|°$) of the

conventional HMI synoptic data by the AI-generated data. For the HMI synoptic data, we use the HMI daily updated radial field synoptic map with polar field correction (Sun et al. 2011). Fourth, we extrapolate coronal magnetic fields from 1 to $2.5R_\odot$ using the PFSS model, with the HMI and AI synchronic data as input. We use pfsspy software package (Stansby et al. 2020) to compute the synchronic PFSS model and trace the magnetic field lines.

3. Results

3.1. Magnetic Field Configurations and Strengths of Source Regions

Figure 2 shows the AI_{HMI}-PFSS, HMI-PFSS, GONG-PFSS, and ADAPT-PFSS extrapolations of the N1 and N2 events, which are shown together because they occurred very close together in time. Figures 3–6 are the PFSS extrapolations for the N3, N4, N5, and N6 events, respectively. The source surface magnetic footpoints of the STEREO-B, Earth, and STEREO-A at $2.5R_\odot$ (crosses in Figures 2–6) are calculated by a Parker spiral approximation using solar wind speeds obtained from ACE Solar Wind Electron Proton Alpha Monitor (SWEPAM; McComas et al. 1998), STEREO Plasma and Suprathermal Ion Composition (PLASTIC; Galvin et al. 2008) measurements at the event start times, and the ballistic backmapping method (Nolte & Roelof 1973; Badman et al. 2020; Macneil et al. 2022).

The six events show that AI_{HMI}-PFSS extrapolations contain significant alterations in coronal magnetic topology and PILs. At least in one example (N1 and N2 events in Figure 2), the alteration to the PIL is clearly not captured by any of the conventional PFSS extrapolations, even in the case of synchronic flux transport modeling (ADAPT). These changes are attributed to variations in the strengths of ARs and the appearance or disappearance of ARs in the farside region. Table 2 shows the number of the ARs in the range of the Stonyhurst heliographic longitude ($|\theta| \geqslant 60°$), where conventional magnetograms replaced by the AI-ones and the polarities of the source regions and the source surface magnetic footpoints of the spacecraft. It also shows the polarities of the SEPx source regions (white squares in Figures 2–6), as well as the polarity of the source surface magnetic footpoints of Earth (yellow crosses), STEREO-A (red crosses), and STEREO-B (blue crosses) at $2.5R_\odot$. There are newly emerged farside ARs for all six events and 1–2 ARs are decayed for the N3 and N6 events in the AI_{HMI}-PFSS model. There are significant variations in the configurations and polarity signs of the magnetic fields connected to the source regions, particularly for the N3, N4, and N6 events, when comparing the AI_{HMI}-PFSS and conventional PFSS extrapolations. The positive open field lines are primarily connected to the newly emerging AR in the AI_{HMI}-PFSS extrapolation of the N3 event. The polarities of the sources for the N4 and N6 differ between the AI_{HMI}-PFSS and the conventional extrapolations. The polarities of the source surface magnetic footpoints of the spacecraft in the AI_{HMI}-PFSS extrapolations are mostly in agreement with those obtained from the conventional extrapolations, with the exception of the N4 event. In addition, we compare the magnetic polarities obtained from in situ measurements with those derived from the four different extrapolations. There are inconsistencies between the in situ measurements and the extrapolations for the N4 event.

Figure 7 shows the source regions of the six events in the AI_{HMI}, HMI, GONG, and ADAPT magnetograms. This figure shows that the source regions have more shaped and more complex magnetic features in the AI-generated maps than those in the conventional maps. By comparing the locations of the source regions, those in the AI_{HMI} magnetograms are mostly consistent with those in the conventional magnetograms but the source regions are more elongated within $\sim10°$ east and westward for the N1, N2, and N6 events, and southward for the N3 event in the AI-generated magnetogram than those in the conventional magnetograms.

Table 3 shows the unsigned total magnetic field fluxes of the source regions for the six events in the AI_{HMI}, the HMI, the GONG, and the ADAPT magnetograms. The quantities computed from all pixels in the field of views are shown in Figure 7. The magnetic fluxes are mostly larger in the AI-generated ones than those in the HMI and GONG maps except for N1 event. For the five events, the differences are between 20% and 140%. In two of the six events, the total fluxes in the AI_{HMI} magnetograms are larger than the ADAPT magnetograms.

3.2. Newly Emerging ARs in the SEP Source Regions

In at least three cases, the AI_{HMI} magnetograms show newly emerged ARs appearing in the vicinity of the previously identified source region and may in fact be the true source of the N3 and N5 events. The source of the N3 event is located behind the west limb (W150°), and it is associated with a fast halo CME with $1319\,\mathrm{km\,s^{-1}}$ at 10:12UT (SOHO LASCO C2 appearance time). In the AI_{HMI}-PFSS magnetogram of Figure 3, the new AR (yellow square) appears very close to the source AR (white square), and the two ARs are connected, as seen in Figure 7(c). In Table 4, the total unsigned magnetic flux of the source, including the new AR is larger in the AI_{HMI} than those in the conventional magnetograms. The fluxes are 3.071×10^{22} Mx in the AI_{HMI}, 1.865×10^{22} Mx in the HMI, 1.347×10^{22} Mx in the GONG, and 2.113×10^{22} Mx magnetogram, respectively. Figure 8 shows the running difference image of the obtained from the EUV synchronic maps (SDO/ AIA 193 Å and STREREO/EUVI 195 Å) combined with magnetic field extrapolations at $2.5R_\odot$, which represents the evolutions of the solar eruptions. Figure 8(c) for the N3 event shows that a solar eruption happened in the newly appeared AR, which implies that the new AR is more likely to be associated with the SEP acceleration.

The N5 event is associated with an M2.9 flare at S16E73° which occurred at 03:14UT on 2013 June 21, and a rapid CME with a linear speed of $1900\,\mathrm{km\,s^{-1}}$, at 03:12UT. The associated eruption was observed on the far east side of the EUV running difference image (see Figure 8(e)). However, in the GONG and HMI magnetograms (Figure 7(e)), noticeable ARs associated with the eruption are not detected at the eruption location. The AI_{HMI} magnetogram reveals the presence of a compact source region whose location is consistent with the observed EUV eruption. Additionally, the ADAPT magnetogram, which benefits from a wide observational range over $\pm 60°$ based on the central meridian, due to data assimilations (Hickmann et al. 2015), also detects the AR at the location of the EUV eruption. ADAPT forward models on the farside (via flux transport) would also play a role in getting features that do not appear in synoptic magnetograms. While the AI_{HMI} magnetogram provides the detailed structures of the source region, the ADAPT magnetogram has limited ability to resolve them.
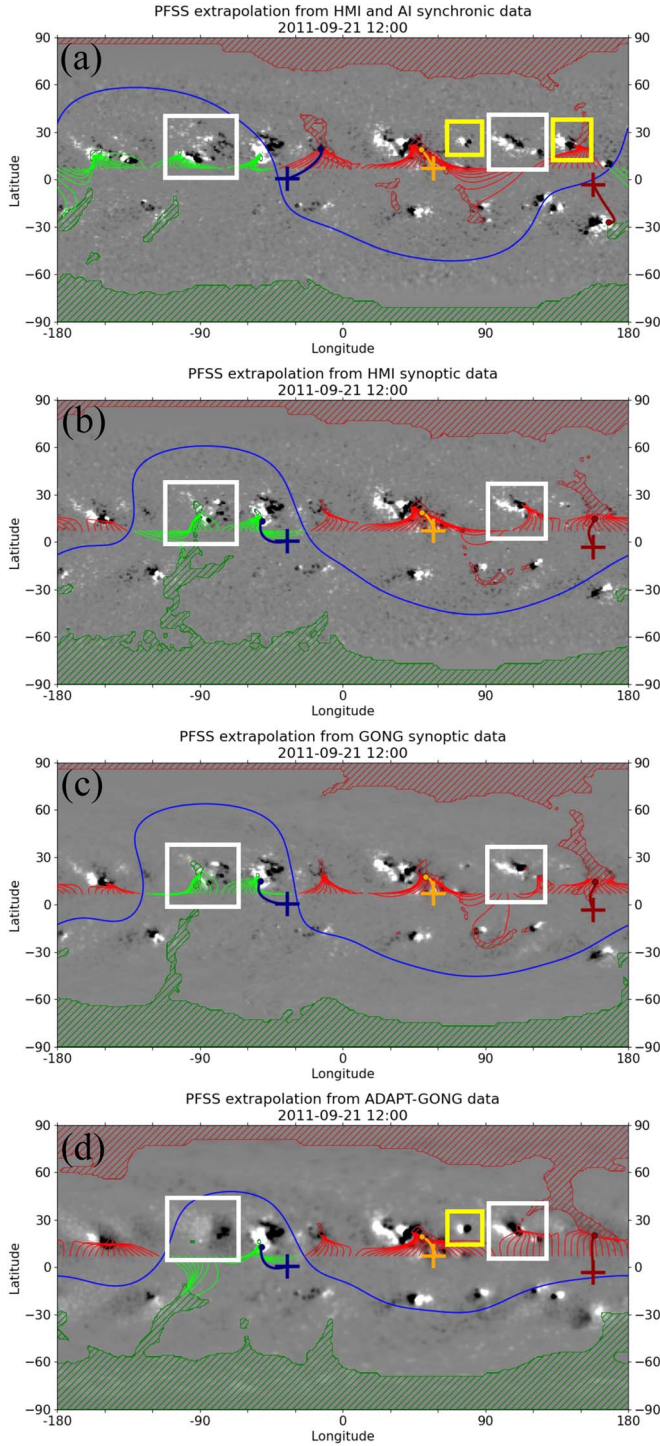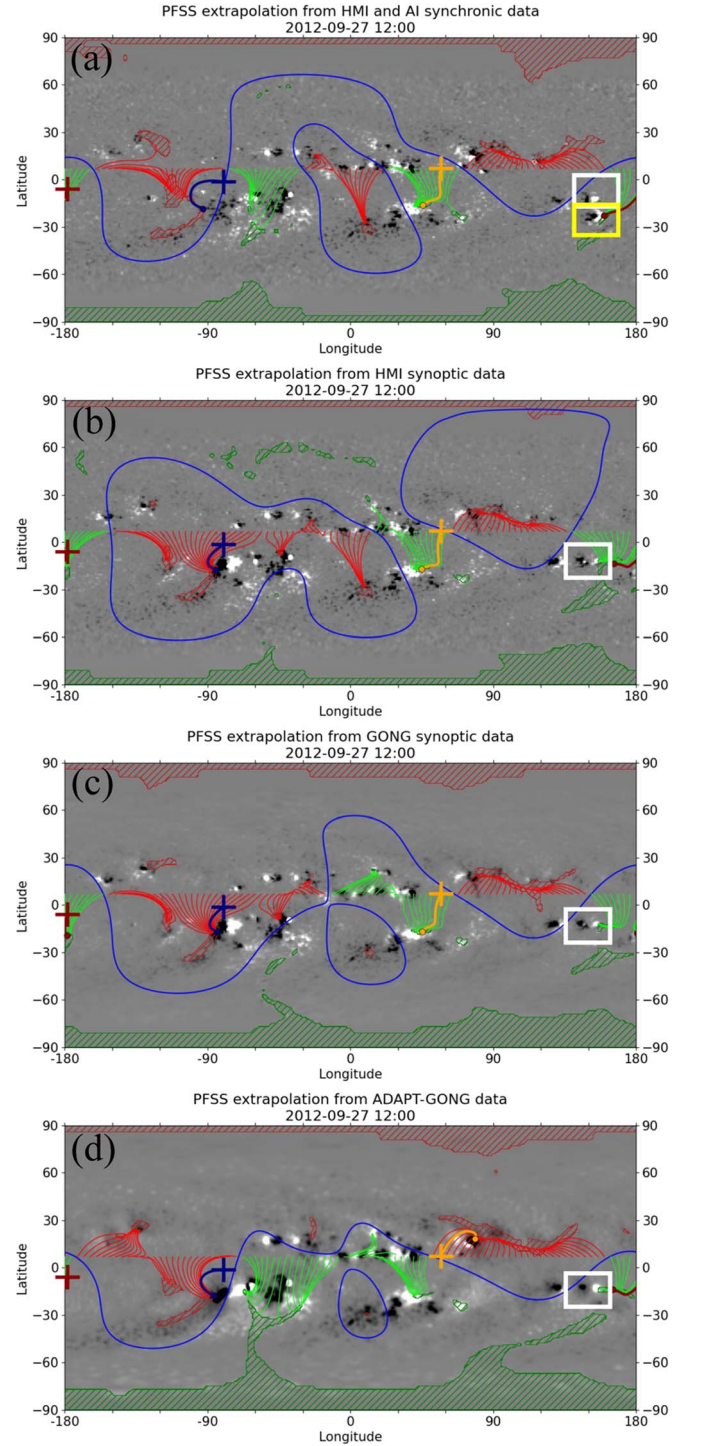
Figure 2. From top to bottom: (a) AI$_{HMI}$-PFSS, (b) HMI-PFSS, (c) GONG-PFSS, and (d) ADAPT-PFSS extrapolations for the N1 and N2 events (2011 September 21 and 22). The red, blue, and yellow crosses represent the magnetic footpoints of STEREO-A, B, and Earth at 2.5$R_\odot$, respectively. The red, blue, and yellow dots represent the photospheric magnetic footpoints of STEREO-A, B, and Earth at 1$R_\odot$, respectively. The blue lines are the PILs. The green and red lines indicate positive and negative open magnetic fields, respectively. The right-hand white square is the source region of the N1 event and the left-hand white square is the source region of the N2 event. Newly observed ARs are enclosed by yellow squares.

In the N1 event, newly generated ARs appear on both the east and west sides of the source region at W120°, as shown in the AI$_{HMI}$-PFSS extrapolation of Figure 2(a). The newly generated ARs are located at a distance of approximately

Figure 3. From top to bottom: (a) AI$_{HMI}$-PFSS, (b) HMI-PFSS, (c) GONG-PFSS, and (d) ADAPT-PFSS extrapolations for the N3 event (2012 September 27). The SEP source region is enclosed by a white square. The newly observed source region is enclosed by a yellow square.

~10°–20° from the source region, and no significant eruptions are detected in the newly generated ARs at the time of the flare and the CME eruptions.

3.3. Polarity Inversion Lines Near the SEP Source Regions

Figure 8 shows the full-Sun running difference images (STEREO-A, B EUVI 195 Å and SDO AIA 193 Å) with the AI$_{HMI}$-PFSS extrapolations. As seen in the figure, the large
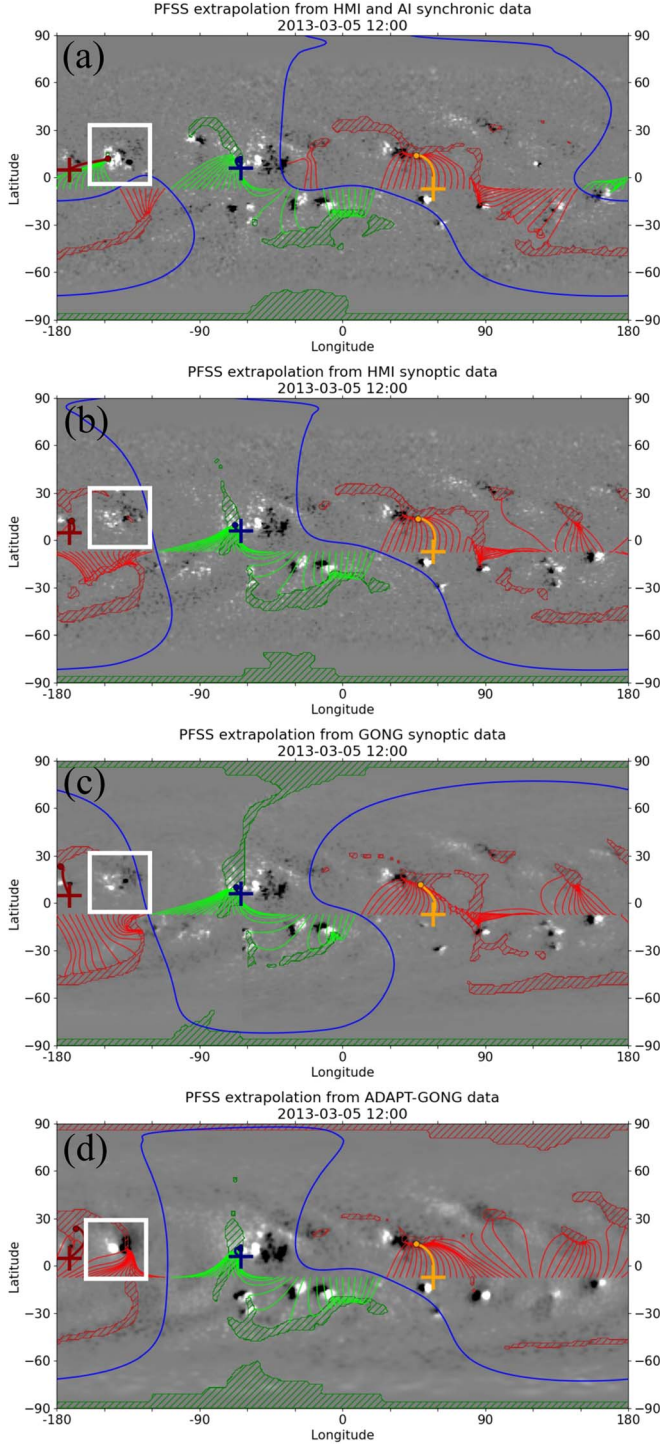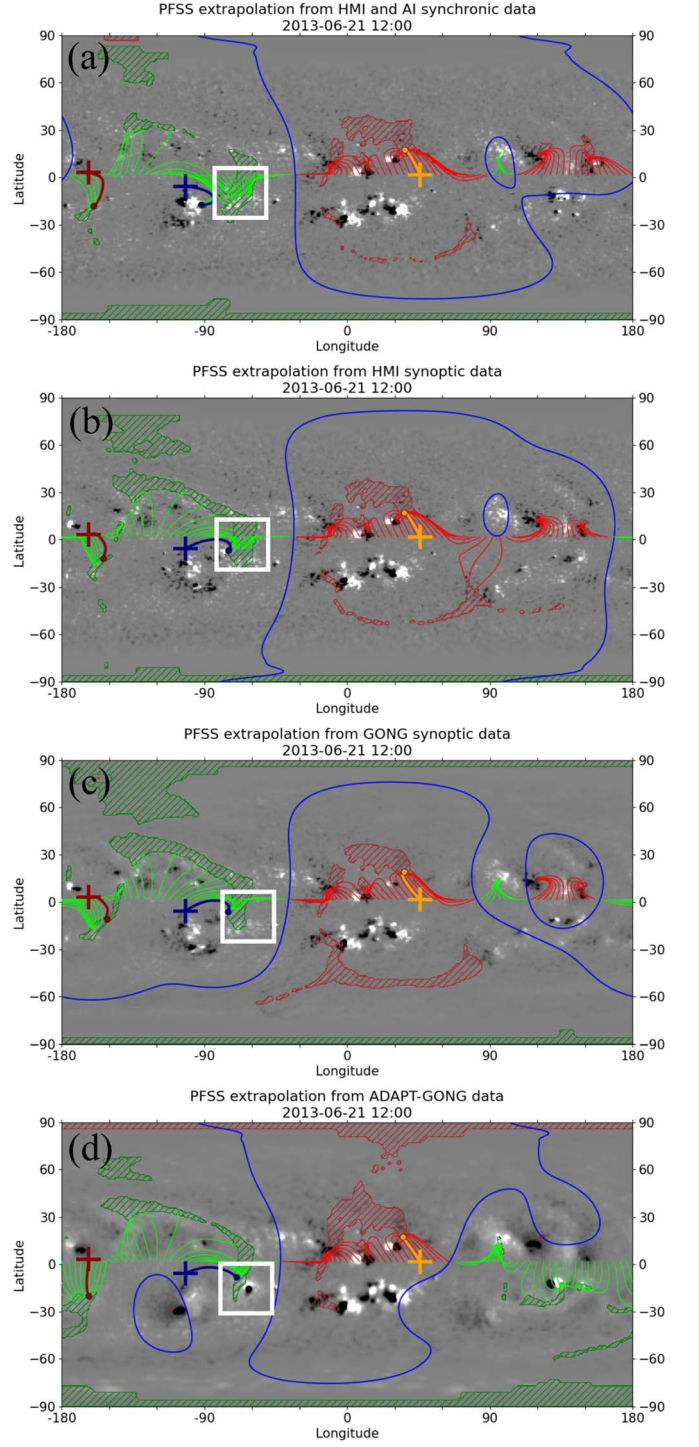
Figure 4. From top to bottom: (a) AI$_{\mathrm{HMI}}$-PFSS, (b) HMI-PFSS, (c) GONG-PFSS, and (d) ADAPT-PFSS extrapolations for the N4 event (2013 March 5). The SEP source region is enclosed by a white square.

Figure 5. From top to bottom: (a) AI$_{\mathrm{HMI}}$-PFSS, (b) HMI-PFSS, and (c) GONG-PFSS, and (d) ADAPT-PFSS extrapolations for the N5 event (2013 June 21). The SEP source region is enclosed by a white square.

disturbances of the EUV waves from the source regions are observed except for the N5 event, which is associated with the small and compact source region compared with the others. The waves are thought of as the signatures of the CME-driven shock in the solar corona region. They appear as faint fronts moving with velocities up to 1000 km s^{-1} in the low corona region being associated with solar eruptions (Moses et al. 1997; Thompson et al. 1998). They can be refracted by ARs and streamers, and attenuated through them.

For the six events in this study, the propagation configurations of the EUV waves are mostly comparable to the configurations of the PILs in the AI$_{\mathrm{HMI}}$-PFSS. In the N4 and N6 events, the PILs near the SEP source regions are different between the AI$_{\mathrm{HMI}}$-PFSS and the other conventional extrapolations. In Figure 8(d), the EUV waves associated with the N4 event mostly propagate from the source region to the northward, and the path is comparable to the configuration of the inversion line in the AI$_{\mathrm{HMI}}$-PFSS extrapolation. The source
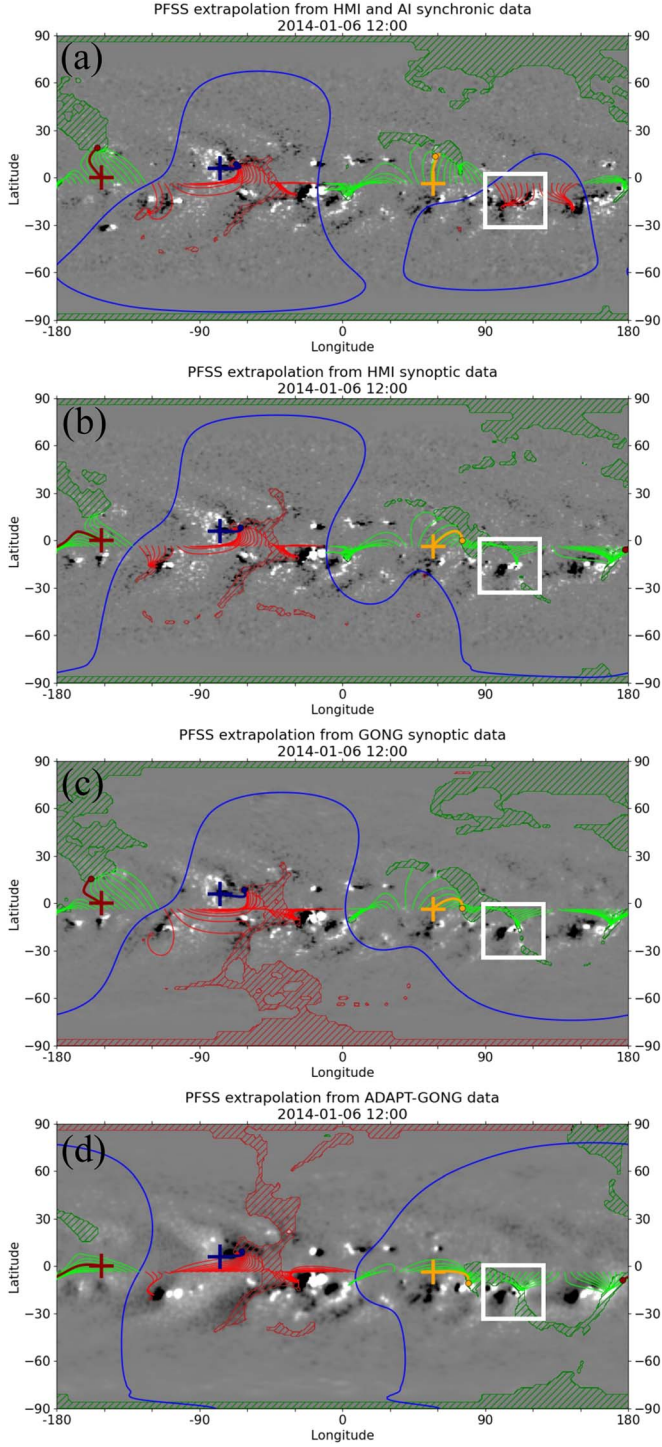
Figure 6. From top to bottom: (a) AI$_{HMI}$-PFSS, (b) HMI-PFSS, and (c) GONG-PFSS, and (d) ADAPT-PFSS extrapolations for the N6 event (the 2014 January 6). The SEP source region is enclosed by a white square.

region of the N6 event is located at W110° enclosed by the white square in Figure 6. The AI$_{HMI}$-PFSS plot shows that the source region is surrounded by the inversion line and the sector of the source region has a negative polarity. Meanwhile, the other extrapolations show the inversion line located down to the source region, and the western region including the source AR has mostly a positive polarity. As seen in Figure 7(f) the large and strong magnetic fields of the source region are generated in the AI$_{HMI}$ magnetogram compared with the

conventional ones, which is may make the negative sector in the western region in the PFSS extrapolations. The EUV wave propagation is typically observed to be oriented nearly perpendicular with respect to the local PIL, suggesting that the AI$_{HMI}$-PFSS extrapolations around the source region are more realistic.

4. Summary and Discussion

In this study, we have examined the global magnetic field configurations for the six SEPs accelerated near or behind the limbs. We have examined the events using the AI$_{HMI}$-PFSS extrapolations, which were developed by Jeong et al. (2022), and the conventional extrapolations (HMI, GONG, and ADAPT-PFSS extrapolations). The main advantage of the AI$_{HMI}$-PFSS extrapolation is that it incorporates realistic near real-time farside magnetic field information informed by EUV data, rather than assuming it is frozen in time (as with HMI and GONG synoptic maps) or forward modeling old data (as with ADAPT synchronic maps). For the AI$_{HMI}$-PFSS extrapolation, the synchronic data, which are constructed by combining frontside SDO/HMI magnetograms and farside AI-generated ones from STEREO/EUVI observations, are used for the input data. Jeong et al. (2020) shows that the global fields in the AI$_{HMI}$ magnetograms are more consistent with limb and farside observations than the conventional magnetic field synoptic data, especially for rapid changes in the magnetic fields by flux emergence or disappearance. We summarize this study as follows.

1. The locations of the source regions are not much different for the six events between the AI$_{HMI}$ and the conventional magnetograms (Figure 7). For the events of the N1, N2, and N6 events, it is seen that the source regions are more elongated within ∼10° east and westward. In the N3 event, the source regions are more elongated within ∼10° southward. The total unsigned magnetic field fluxes of the source ARs are mostly stronger in the AI$_{HMI}$ magnetogram than those in the HMI and GONG magnetograms, except for one event. In two of the six events, the total fluxes in the AI$_{HMI}$ magnetograms are larger than the ADAPT magnetograms.

2. Newly emerged ARs in the SEP source regions are observed in the AI$_{HMI}$-PFSS for N3 and N5 events. For the N3 event, the location of the emission features in the running difference images from full-Sun EUV synchronic maps is more consistent with the location of the newly generated AR in the AI$_{HMI}$-PFSS extrapolation. For the N5 event, the source region is detected at S16E73° in the EUV observation and the compact AR is generated at the location in the AI$_{HMI}$ magnetogram, but there is no noticeable AR at the location in the HMI and GONG-PFSS magnetogram. The ADAPT magnetogram detects the AR due to the data assimilation method, but it is hard to examine the detailed structure for the AR. This implies that these source regions are likely to continue to strengthen. They can be expected to have an impact on the coronal topology and are likely to host eruptive events.

3. The PILs are changed due to the appearance and/or the disappearance of the ARs. In the running difference EUV images for the six events, the propagation directions of the source eruptions are compared to the configurations of the PILs in the AI$_{HMI}$-PFSS extrapolations. For the N4

Table 2
The Number of the ARs in the Range of the Stonyhurst Heliographic Longitude ($|\theta| \geqslant 60°$), the Polarities of the Source Regions, and the Polarities of the Spacecraft Source Surface Footpoints at $2.5R_\odot$ (S_f) in the AI_{HMI}-PFSS, HMI-PFSS, GONG-PFSS, and ADAPT-PFSS Extrapolations for the Six SEP Events

No. (1)	Data (2)	AR_n				Source Polarity				S_f Polarity (B, E, A)					Obs (16)
		AI_{HMI} (3)	HMI (4)	GONG (5)	ADAPT (6)	AI_{HMI} (7)	HMI (8)	GONG (9)	ADAPT (10)	AI_{HMI} (11)	HMI (12)	GONG (13)	ADAPT (14)	In Situ (15)	
N1	20110921	13 (4,0)	9	9	10	N	N	N	N	PN N* PN	P* N* N*	PN N* N*	P* N* PN	P N N	S,A
N2	20110922	13 (4,0)	9	9	10	P	P	P	P	PN N* PN	P* N* N*	PN N* N*	P* N* PN	P N N	B,S(G),A
N3	20120927	7 (1,1)	7	7	6	P	P	P	P	PN PN P	N PN P	N PN P	PN PN P	P N PN	B,S(G),A
N4	20130305	7 (2,0)	5	5	5	P	N	N	N	P N* P	P N* N*	P N* N*	P N* N*	N N N	B,S,A
N5	20130621	7 (1,0)	6	6	6	P	P	P	P	P* N* P	P* N* P	P* N* P	P* N* P	P N P	B,S(G),A
N6	20140106	6 (2,2)	6	6	6	N	P	P	P	N P* P	N P* P	N P* P	N P* P	PN P PN	B,S(G),A

Note. The numbers in the parenthesis represent newly generated ARs and degenerated ARs in the AI_{HMI}-PFSS extrapolations. Spacecraft detecting the SEP events are listed in column 16. G, S, A, and B represent GOES/EPEAD, SOHO/EREN, STEREO-A/LET, and STEREO-B/LET, respectively. Spacecraft that are underlined indicate that the source surface footpoints are closest to the source regions. * The single polarities in columns 11–14 are agree with in situ observation in column 15.
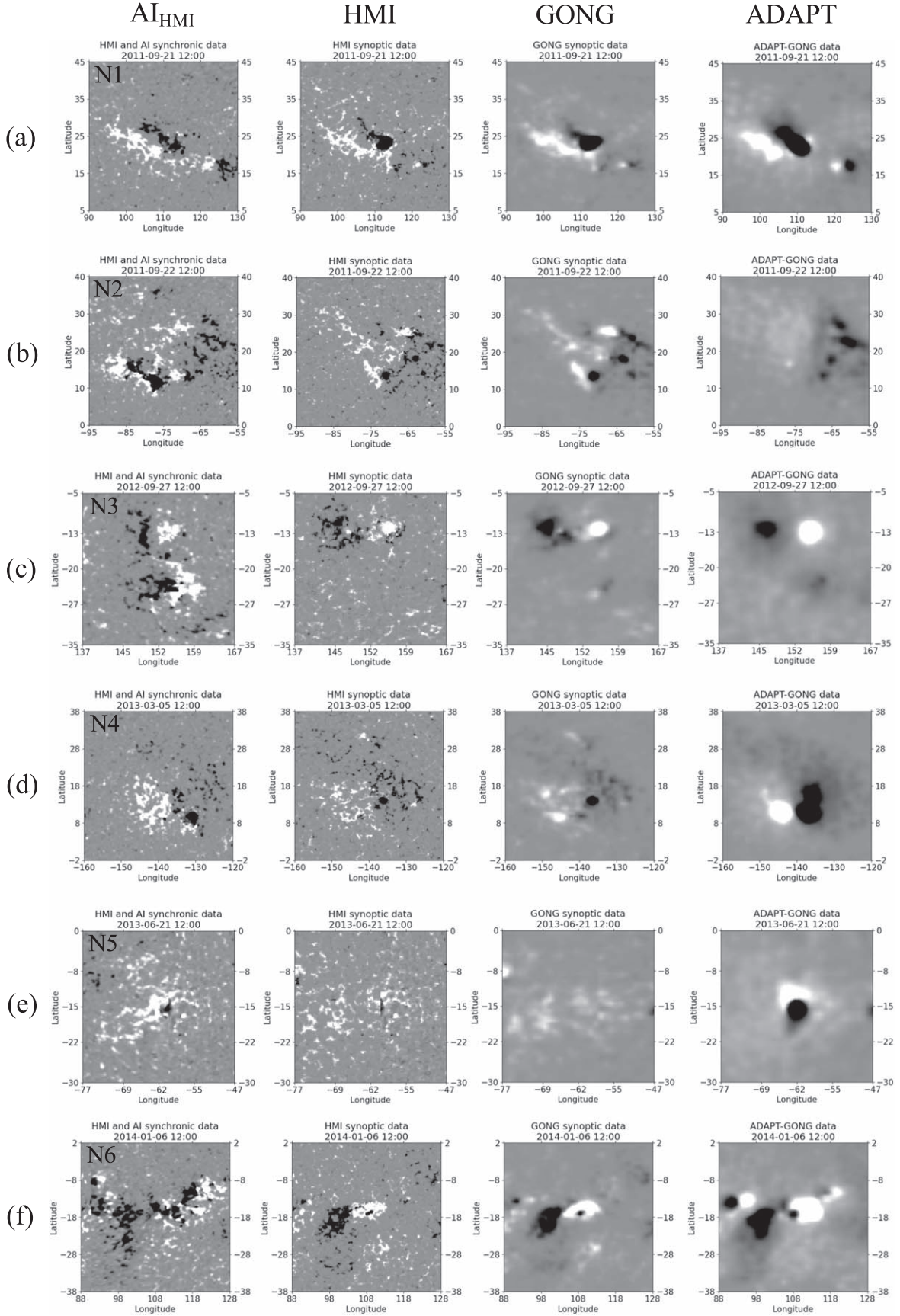
Figure 7. The source regions of the six events in the AI$_{HMI}$, HMI, GONG, and ADAPT magnetograms: (a) the N1 event (2011 September 21), (b) the N2 event (2011 September 22), (c) the N3 event (2012 September 27), (d) the N4 event (2013 March 5), (e) the N5 event (2013 June 21), and (f) the N6 event (2014 January 6).
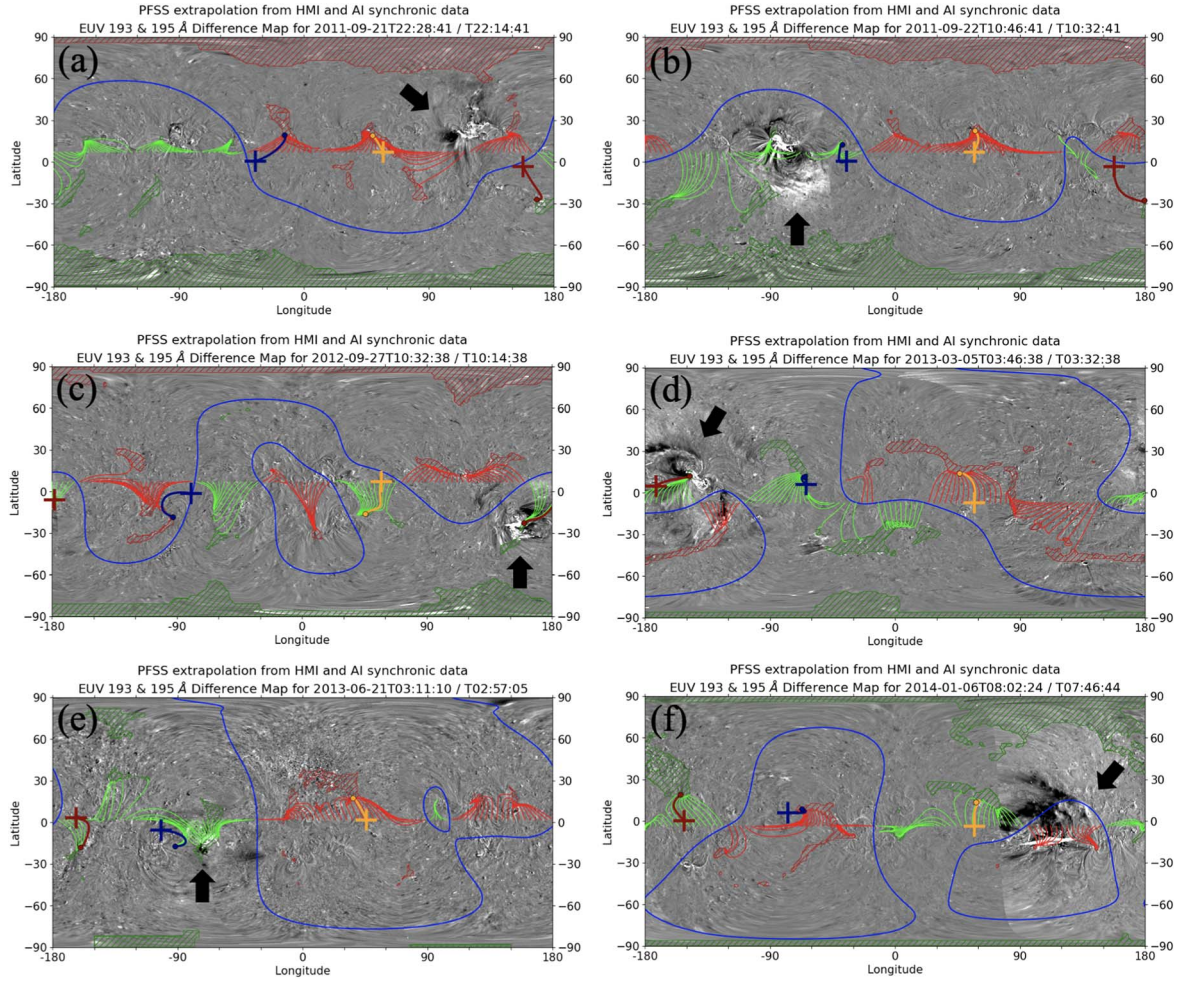
Figure 8. The full-Sun running difference images (STEREO-A, B EUVI 195 Å and SDO AIA 193 Å) with the AI$_{HMI}$-PFSS extrapolations at the times given: (a) the N1 event (2011 September 21), (b) the N2 event (2011 September 22), (c) the N3 event (2012 September 27), (d) the N4 event (2013 March 5), (e) the N5 event (2013 June 21), and (f) the N6 event (2014 January 6). The black arrows indicate EUV wave propagations associated with the SEP events.

Table 3
Total Unsigned Magnetic Fluxes of the Source Regions from AI$_{HMI}$, HMI, GONG, and ADAPT Magnetograms for the Six SEP Events

No.	Data	Longitude	Latitude	AI$_{HMI}$ ($\times 10^{22}$Mx)	HMI ($\times 10^{22}$Mx)	GONG ($\times 10^{22}$Mx)	ADAPT ($\times 10^{22}$Mx)	[a][AI, HMI]	[b][AI, GONG]	[c][AI, ADAPT]
(1)	(2)	(3)	(4)	(5)	(6)	(7)	(8)	(9)	(10)	(11)
N1	20110921	$[+110° \pm 20°]$	$[+25° \pm 20°]$	3.405	3.946	2.783	5.160	−13.72%	22.34%	−34.00%
N2	20110922	$[-75° \pm 20°]$	$[+20° \pm 20°]$	5.491	3.167	2.316	2.739	73.37%	137.05%	100.49%
N3	20120927	$[+152° \pm 15°]$	$[-20° \pm 15°]$	3.071	1.865	1.347	2.113	64.66%	127.98%	45.37%
N4	20130305	$[-140° \pm 20°]$	$[+18° \pm 20°]$	3.535	2.652	1.851	5.393	33.29%	90.99%	−34.46%
N5	20130621	$[-62° \pm 15°]$	$[-15° \pm 15°]$	2.100	1.714	1.172	2.617	22.50%	79.14%	−19.76%
N6	20140106	$[+108° \pm 20°]$	$[-18° \pm 20°]$	5.717	3.834	2.888	6.240	49.12%	97.98%	−8.37%

Notes.
[a] [AI,HMI] = (AI-HMI)/HMI*100.
[b] [AI,GONG] = (AI-GONG)/GONG*100.
[c] [AI,ADAPT] = (AI-ADAPT)/ADAPT*100.

and N6 events, the magnetic polarity sectors containing the source ARs are changed.

4. In five out of the six events, when accounting for all footpoints including those near the PILs having mixed polarities, the footpoint polarities in the AI$_{HMI}$-PFSS extrapolations remain consistent with the modeled polarities. Furthermore, in these five out of six events,

the polarities of the footpoints in the AI$_{HMI}$-PFSS extrapolations correspond to the polarities measured in situ.

In this study, we cannot rule out uncertainties in determining the source surface magnetic footpoints of the spacecraft. Nolte & Roelof (1973) showed that the longitudes of the source

surface magnetic footpoints could be determined with an accuracy of $10°$ using the Parker spiral approximation. Kahler et al. (2016) found that the footpoints on photospheric and $5R_\odot$ source longitudes from Parker spiral field approximation are consistent with those from Wang-Sheeley-Arge within several degrees but not in the slow-fast solar wind interaction regions.

In terms of the space-weather forecast, SEPs accelerated behind the limbs are important for the observers on the Sun-Earth line. The observers can be magnetically connected to the SEP sources behind the limbs. In particular, there is a high possibility of directly connecting the SEPs near and behind the west limb. When considering the limitation of the farside observation in the conventional models, the AI_{HMI}-PFSS model is able to give a better understanding of SEP source regions near and behind limbs, and their magnetic field connections.

Acknowledgments

ORCID iDs

Jinhye Park https://orcid.org/0000-0002-0678-2969
Hyun-Jin Jeong https://orcid.org/0000-0003-4616-947X
Yong-Jae Moon https://orcid.org/0000-0001-6216-6944

References

Altschuler, M. D., & Newkirk, G. 1969, SoPh, 9, 131
Arge, C. N., & Pizzo, V. J. 2000, JGR, 105, 10465
Badman, S. T., Bale, S. D., Martínez Oliveros, J. C., et al. 2020, ApJS, 246, 23
Bučík, R. 2020, SSRv, 216, 24
Cane, H. V., Mewaldt, R. A., Cohen, C. M. S., & von Rosenvinge, T. T. 2006, JGRA, 111, A06S90
Galvin, A. B., Kistler, L. M., Popecki, M. A., et al. 2008, SSRv, 136, 437
Gopalswamy, N. 2003, GeoRL, 30, 8013
Gopalswamy, N., Yashiro, S., Akiyama, S., et al. 2008, AnGeo, 26, 3033
Hickmann, K. S., Godinez, H. C., Henney, C. J., & Arge, C. N. 2015, SoPh, 290, 1105
Howard, R. A., Moses, J. D., Vourlidas, A., et al. 2008, SSRv, 136, 67
Jeong, H.-J., Moon, Y.-J., Park, E., & Lee, H. 2020, ApJL, 903, L25
Jeong, H.-J., Moon, Y.-J., Park, E., Lee, H., & Baek, J.-H. 2022, ApJS, 262, 50
Kahler, S. 1994, ApJ, 428, 837
Kahler, S. W. 2001, JGR, 106, 20947
Kahler, S. W., Arge, C. N., & Smith, D. A. 2016, SoPh, 291, 1829
Kahler, S. W., & Vourlidas, A. 2013, ApJ, 769, 143
Kallenrode, M.-B. 2003, JPhG, 29, 965
Laker, R., Horbury, T. S., Bale, S. D., et al. 2021, A&A, 652, A105
Lemen, J. R., Title, A. M., Akin, D. J., et al. 2012, SoPh, 275, 17
Macneil, A. R., Owens, M. J., Finley, A. J., & Matt, S. P. 2022, MNRAS, 509, 2390
McComas, D. J., Bame, S. J., Barker, P., et al. 1998, SSRv, 86, 563
Mewaldt, R. A., Cohen, C. M. S., Cook, W. R., et al. 2008, SSRv, 136, 285
Moses, D., Clette, F., Delaboudinière, J.-P., et al. 1997, SoPh, 175, 571
Nolte, J. T., & Roelof, E. C. 1973, SoPh, 33, 241
Park, J., Innes, D. E., Bucik, R., & Moon, Y.-J. 2013, ApJ, 779, 184
Park, J., Innes, D. E., Bucik, R., Moon, Y.-J., & Kahler, S. W. 2015, ApJ, 808, 3
Park, J., Moon, Y.-J., & Gopalswamy, N. 2012, JGRA, 117, 8108
Reames, D. V. 1998, SSRv, 85, 327
Reames, D. V. 1999, SSRv, 90, 413
Reames, D. V. 2013, SSRv, 175, 53
Reames, D. V. 2020, SSRv, 216, 20
Riley, P., Linker, J. A., Mikić, Z., et al. 2006, ApJ, 653, 1510
Schatten, K. H., Wilcox, J. M., & Ness, N. F. 1969, SoPh, 6, 442
Stansby, D., Yeates, A., & Badman, S. T. 2020, JOSS, 5, 2732
Sun, X., Liu, Y., Hoeksema, J., Hayashi, K., & Zhao, X. 2011, SoPh, 270, 9
Thompson, B. J., Plunkett, S. P., Gurman, J. B., et al. 1998, GeoRL, 25, 2465
Torsti, J., Valtonen, E., Lumme, M., et al. 1995, SoPh, 162, 505
Tylka, A. J., & Lee, M. A. 2006, ApJ, 646, 1319
vonRosenvinge, T. T., Reames, D. V., Baker, R., et al. 2008, SSRv, 136, 391
Wang, Y.-M., & Sheeley, N., Jr 1992, ApJ, 392, 310